






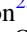





The Prospect of Detecting Volcanic Signatures on an ExoEarth Using Direct Imaging

Colby M. Ostberg^{1,2} , Scott D. Guzewich^{2,3} , Stephen R. Kane¹ , Erika Kohler² , Luke D. Oman^{2,3} ,
Thomas J. Fauchez^{2,3,4} , Ravi K. Kopparapu^{2,3} , Jacob Richardson^{2,3} , and Patrick Whelley^{2,3,5} 

¹Department of Earth and Planetary Sciences, University of California, Riverside, CA 92521, USA; costb001@ucr.edu

²NASA Goddard Space Flight Center, 8800 Greenbelt Road, Greenbelt, MD 20771, USA

³Sellers Exoplanet Environments Collaboration, NASA Goddard Space Flight Center, 8800 Greenbelt Road, Greenbelt, MD 20771, USA

⁴Integrated Space Science and Technology Institute, Department of Physics, American University, Washington, DC, USA

⁵University of Maryland, Department of Astronomy, College Park, MD 20742, USA

Received 2023 June 26; revised 2023 September 12; accepted 2023 September 26; published 2023 October 19

Abstract

The James Webb Space Telescope (JWST) has provided the first opportunity of studying the atmospheres of terrestrial exoplanets and estimating their surface conditions. Earth-sized planets around Sun-like stars are currently inaccessible with JWST, however, and will have to be observed using the next generation of telescopes with direct-imaging capabilities. Detecting active volcanism on an Earth-like planet would be particularly valuable as it would provide insight into its interior and provide context for the commonality of the interior states of Earth and Venus. In this work, we used a climate model to simulate four exoEarths over eight years with ongoing large igneous province eruptions with outputs ranging from 1.8 to 60 Gt of sulfur dioxide. The atmospheric data from the simulations were used to model direct-imaging observations between 0.2 and 2.0 μm , producing reflectance spectra for every month of each exoEarth simulation. We calculated the amount of observation time required to detect each of the major absorption features in the spectra, and we identified the most prominent effects that volcanism had on the reflectance spectra. These effects include changes in the size of the O₃, O₂, and H₂O absorption features and changes in the slope of the spectrum. Of these changes, we conclude that the most detectable and least ambiguous evidence of volcanism are changes in both O₃ absorption and the slope of the spectrum.

Unified Astronomy Thesaurus concepts: [Exoplanet atmospheres \(487\)](#); [Exoplanet astronomy \(486\)](#); [Exoplanet detection methods \(489\)](#); [Exoplanets \(498\)](#); [Volcanism \(2174\)](#); [Direct imaging \(387\)](#); [Spectroscopy \(1558\)](#)

1. Introduction

The atmospheres of terrestrial exoplanets have become increasingly accessible through the use of both transmission and emission spectroscopy (Seager & Deming 2010; Madhusudhan 2019), particularly in the era of the James Webb Space Telescope (JWST; Beichman et al. 2014; Greene et al. 2016; Bean et al. 2018; Fortenbach & Dressing 2020). Emission spectroscopy and thermal infrared phase curves have been used to determine whether exoplanets have atmospheres (e.g., Kreidberg et al. 2019; Kane et al. 2020; Greene et al. 2023), while transmission spectroscopy is capable of identifying the molecular species in exoplanet atmospheres (e.g., Tinetti et al. 2010; Sing et al. 2011; Fraine et al. 2014; Ridden-Harper et al. 2023). These techniques provide vital information that can be input into three-dimensional (3D) general circulation models (GCMs) to estimate the potential climate states of exoplanets (e.g., Turbet et al. 2016, 2018; Wolf 2017; Wolf et al. 2017; Fauchez et al. 2021). Refining estimates of exoplanet climates will require understanding the states of both the atmosphere and the interior of a planet because geological activity has been a crucial component for Earth to maintain habitable conditions throughout its history.

Determining the geological properties of an exoplanet by studying its surface is a challenging task with current technologies. Therefore, inferring the state of exoplanet interiors will largely rely on indirect techniques, such as

through the study of planetary atmospheres (Kislyakova et al. 2017; Guenther & Kislyakova 2020; Harnett et al. 2020; Quick et al. 2020; Noack et al. 2021). Detection of volcanic compounds such as methane (CH₄), carbon dioxide (CO₂), and sulfur dioxide (SO₂) would provide insight into potential volcanic activity occurring on an exoplanet (e.g., Kaltenegger et al. 2010; Hu et al. 2013; Misra et al. 2015; Loftus et al. 2019; Fortin et al. 2022). Detection of SO₂ in an exoEarth atmosphere would be a particularly strong indication of ongoing volcanism due to its short chemical lifetime in an Earth-like atmosphere. Atmospheric CO₂ has a much longer lifetime than SO₂ and is evidence of outgassing, but it would be difficult to constrain whether the outgassing occurred recently or in the past. CH₄ also has a short lifetime in Earth's atmosphere, but would require either substantial volcanism or living organisms in order for detectable amounts of CH₄ to be sustained (e.g., Krissansen-Totton et al. 2018, 2022; Thompson et al. 2022). JWST has the capability of probing the atmospheres of terrestrial planets, but is limited to those that orbit cooler, smaller stars such as M dwarfs. Observing the atmosphere of an Earth-like planet around a Sun-like star will require future direct-imaging missions like the Habitable Worlds Observatory, which is based on the HabEx (Gaudi et al. 2020) and LUVOIR (The LUVOIR Team et al. 2019) mission concepts, and the Large Interferometer For Exoplanets, which would be sensitive enough to directly image planets around M dwarfs (Quanz et al. 2022).

In this work, we investigate the potential of detecting evidence of volcanism in the reflectance spectra of an exoEarth. This involves using a 3D GCM to simulate volcanic eruptions of varying sizes on an exoEarth, identifying how volcanism



Original content from this work may be used under the terms of the [Creative Commons Attribution 4.0 licence](#). Any further distribution of this work must maintain attribution to the author(s) and the title of the work, journal citation and DOI.

affects the reflectance spectra of each eruption, and simulating observations with a LUVOIR-like telescope. In Section 2 we describe the 3D GCM used to model eruptions, and how we simulated the reflectance spectra and observations of the exoEarth. Section 3 describes the results of the signal-to-noise ratio (S/N) analysis and the maximum and minimum observation time needed to detect individual features. In Section 4 we discuss the features and bandpasses that should be prioritized in future observations, and we list the caveats of the study. Concluding remarks and future work that is needed are discussed in Section 5.

2. Methods

2.1. GEOSCCM Global Climate Model

The Goddard Earth Observing System Chemistry Climate Model (GEOSCCM) simulates Earth’s modern climate using coupled atmospheric general circulation and dynamic ocean models (Rienecker et al. 2008; Nielsen et al. 2017; Aquila et al. 2021). It additionally uses the Global Modeling Initiative stratosphere–troposphere chemical routine (Duncan et al. 2007; Strahan et al. 2007), which integrates a bulk aerosol module (Goddard Chemistry, Aerosol, Radiation, and Transport: GOCART; Colarco et al. 2010). In combination, this allows GEOSCCM to self-consistently simulate climate, cloud, chemistry, and aerosol physics. Simulations were run at $1^\circ \times 1^\circ$ horizontal resolution in both the ocean and the atmosphere, with 72 vertical layers in the atmosphere extending to 80 km altitude and 50 ocean layers to a depth of 4.5 km. The initial and boundary conditions of the model are identical to the modern pre-industrial Earth and Sun with fixed CO₂ concentrations of 280 ppm.

Our simulations modeled the climate impact of large igneous province (LIP; also known as “flood basalt”) volcanism (Courtillot & Renne 2003; Self et al. 2006; Bryan et al. 2010; Bond & Sun 2021). Specifically, it modeled the Columbia river flood basalt eruption, which is geologically the most recent (15–17 Ma) and smallest known such eruption in terrestrial history (McKay et al. 2014; Kasbohm & Schoene 2018). Flood basalt volcanism is believed to occur on every other terrestrial world in the solar system (Lancaster et al. 1995; O’hara 2000; Jaeger et al. 2010; Head et al. 2011). The model simulates such an eruption by injecting SO₂ in both the near-surface atmosphere and the upper troposphere-lower stratosphere over the course of 4 yr at two model grid points in eastern states of Oregon and Washington, USA.

We simulated six eruptions that varied from 1.875 to 60 Gt of emitted SO₂, and a baseline case with no SO₂ release. The SO₂ output of the simulated eruptions is similar to that of the 1815 Tambora eruption (Stothers 1984) and the Toba volcano in Sumatra (Oppenheimer 2002). For reference, the yearly global output of SO₂ from volcanos on Earth is estimated to be 0.01 Gt (Stoiber & Jepsen 1973). After the SO₂ is emitted in the simulations, the SO₂ can be oxidized by O₂ and hydroxide (OH), and then combined with water (H₂O) to form sulfuric acid aerosols (H₂SO₄; hereafter referred to as volcanic aerosol). This can occur in the model at any pressure where the chemistry is suitable.

Additional details of the volcanic eruption scenario and GEOSCCM as it was used here are provided by Guzewich et al. (2022). In brief, explosive eruptions (placing SO₂ into the upper troposphere and lower stratosphere) occur once every

three months for the first four simulated years with near-surface effusive eruptions continuing throughout those 4 yr. The eruptions stop after the first 4 yr, and the simulations were ran for an additional 4 yr to examine any lasting changes to the climate system.

Each of the five (four volcanic and one baseline) simulations are run for a total of eight simulated years with variables output as monthly averages. For our purposes of evaluating the planetary reflected-light spectrum, monthly average values better represent the expected spectral changes caused by aerosols, clouds, and variable gas abundances due to the eruption and the subsequent climate impacts rather than changes caused by weather on the timescales of hours to days.

The globally averaged temperature-pressure profiles for every 12 months of the 30 Gt eruption simulation and the single year of the baseline simulation are shown in the upper panel of Figure 1. The volcanic aerosols heat up the upper troposphere and lower stratosphere, which remove the tropopause seen in the baseline TP profile. The eruptions also lead to depletion of O₃, which causes the upper atmosphere to be much cooler in the eruption simulation than in that of the baseline simulation. After the eruptions cease, the tropopause inversion begins to return near the end of the eruption simulation as the volcanic aerosols are slowly removed and O₃ is replenished. The eruptions also move a large amount of H₂O vapor into the troposphere and stratosphere, as shown in the middle panel of Figure 1, which also contributes to the removal of the tropopause. The lower panel of Figure 1 illustrates the large increase in volcanic aerosols during the first 4 yr of the simulation and the slow decrease in volcanic aerosols throughout the last 4 yr of the simulation.

2.2. GlobES and PSG

In order to model the reflected-light spectra of the GEOSCCM exoEarths, we input the monthly averaged outputs into the Global Emission Spectra (GlobES⁶) application, which is part of the Planetary Spectrum Generator (PSG⁷) radiative transfer suite. GlobES uses the 3D TP and chemical abundance data from GCMs, which allows it to incorporate the effects of an inhomogenous atmosphere and surface on reflected-light spectra.

We modeled a timeline of reflectance spectra for each of the four volcanically active exoEarths and the baseline exoEarth. All exoEarths were defined to have Earth’s radius and mass with a circular orbit at 1 au around a Sun-like star that is 10 pc away. The inclination of the system was defined to be edge-on, and the planet had a phase angle of 90° in reference to the observer. The atmosphere of each exoEarth was defined using their monthly averaged atmospheres. Each volcanic exoEarth was simulated for 96 months, giving them 96 reflectance spectra each. The baseline exoEarth was only simulated for 12 months, so it has 12 reflectance spectra.

We assumed that the exoEarth is observed by a hypothetical LUVOIR-B telescope with a 6 m mirror and attached coronagraph. Observational noise was simulated for the ultraviolet (UV), visible (VIS), and near-infrared (NIR) instruments, which have bandpasses of 0.2–0.515, 0.515–1.0, and 1.01–2.0 μm, respectively. All simulated observations consisted of a single 1 hr exposure. The uncertainty of longer

⁶ <https://psg.gsfc.nasa.gov/apps/globes.php>

⁷ <https://psg.gsfc.nasa.gov>

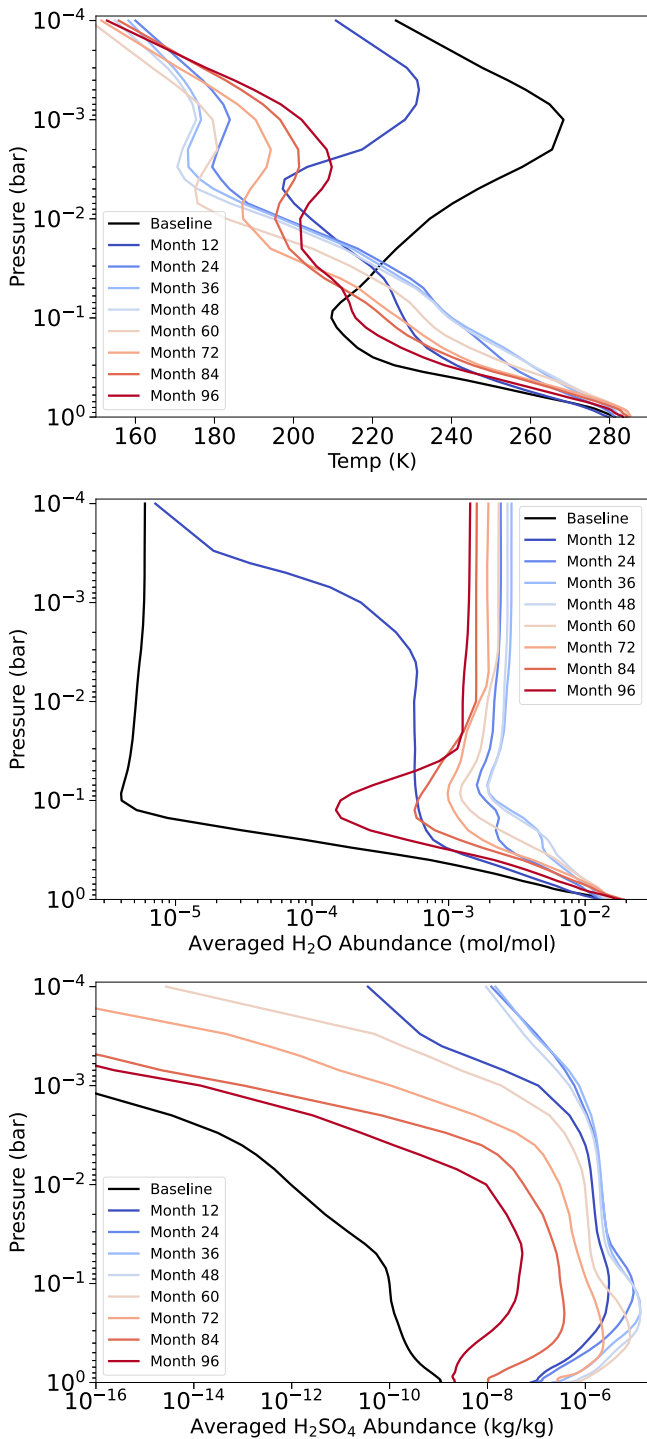


Figure 1. The globally averaged TP profiles (upper panel), H₂O vapor abundance profiles (middle panel), and volcanic aerosol abundance profiles (lower panel) of the 30 Gt eruption exoEarth for every 12 months of the simulation. The corresponding profile of the baseline simulation is shown for reference.

observations was extrapolated using a scaling relationship that is explained in more detail in Section 2.3. The values for instrument-related input parameters were the same as those used in Checlair et al. (2021), which were chosen using the LUVOR final report (The LUVOR Team et al. 2019). The instrument inputs were also similar to that of Kopparapu et al. (2021), who modeled observations of LUVOR-A.

The atmospheric parameters used as inputs for GlobES include 3D TP, molecular abundance, and aerosol abundance profiles. The gas species include H₂O vapor, CO₂, ozone (O₃), nitrous oxide (N₂O), SO₂, CH₄, oxygen (O₂), and nitrogen (N₂). The aerosol species include volcanic aerosol, H₂O aerosol, and water ice. Figure 2 shows the reflectance spectra and corresponding molecular transmittance of the 30 Gt eruption exoEarth atmosphere during month 11 of the simulation. The UV bandpass is dominated by O₃ absorption, but also contains O₂ and SO₂ absorption bands. The SO₂ absorption around 0.3 μm is present during the first 4 yr of the simulations while volcanism is ongoing, but it is always overshadowed by the O₃ and O₂ absorption bands that it overlaps. The VIS bandpass includes absorption by O₂ at 0.75 μm, smaller H₂O features that straddle the O₂ feature, and a larger H₂O feature at 0.95 μm. The NIR bandpass has 3 H₂O absorption features at 1.15, 1.4, and 1.9 μm. During this month, H₂O and volcanic aerosols are also present. They inhibit the size of the H₂O absorption features.

2.3. Calculating the S/N of Spectral Features

We computed the S/N of the major molecular features found in the UV, VIS, and NIR bandpasses in order to quantify their detectability. We chose to focus on calculating the S/N for the O₃ feature in the UV bandpass, for the O₂ and H₂O features in the VIS bandpass, and for the H₂O features in the NIR bandpass. The S/N calculated for the H₂O features in the VIS and NIR bandpasses is the combined S/N of all H₂O features in the given bandpass. To determine the S/N of each feature, we used Equation (1), which is a χ^2 approach used previously by Lustig-Yaeger et al. (2019),

$$S/N = \sqrt{\sum_i^{N_M} \left(\frac{y_i - y_{\text{cont}}}{\sigma_i} \right)^2}. \quad (1)$$

In Equation (1), y_i is the i th y value of the modeled spectrum within the given instrument bandpass, σ_i is the corresponding uncertainty of the simulated data, and y_{cont} is the continuum of the spectrum, which we defined to be the same spectrum, but without absorption from the molecule of interest. Figure 3 shows the continua used to calculate the S/N of the respective features in the UV, VIS, and NIR bandpasses. The S/N of each feature was first calculated for 1 hr of observation, then a scaling relationship was used to extrapolate the S/N of longer observations in 1 hr intervals assuming a photon-noise-limited scenario. The S/N values estimated by the scaling relationship were compared to the S/N values from fully computing the noise of the data. Both methods yielded very similar S/N values, so we opted to use the scaling relationship for all S/N calculations because it is much faster.

We defined the threshold for the detection of a feature to be when the S/N equals or exceeds a value of 5, which is the same threshold as was used in previous studies (e.g., Lustig-Yaeger et al. 2019; Pidhorodetska et al. 2020; Felton et al. 2022). The observation time required to detect individual features was calculated for every monthly averaged spectrum in all eruption cases. The detection of molecules from actual observations will require a more complex analysis with retrieval algorithms and model comparisons. Therefore, the observation times needed for detection reported in this work are to be considered as lower limits.

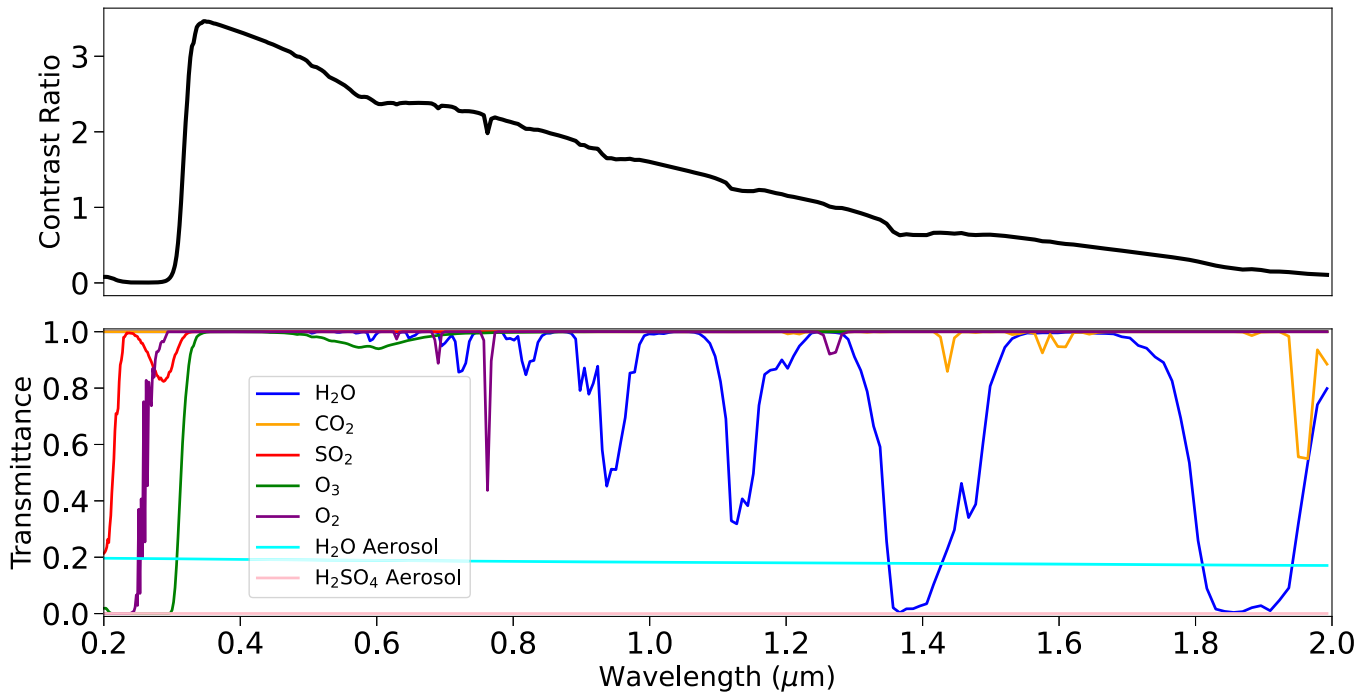


Figure 2. The reflectance spectra of the 30 Gt eruption exoEarth in month 11 of the simulation (upper panel) and the transmittances of the major molecular species in its atmosphere (lower panel). The most prominent absorption feature in the UV is caused by O_3 . Absorption by SO_2 occurs in the UV around $0.3 \mu\text{m}$, but it is overshadowed by O_3 and O_2 absorption. The VIS bandpass has a single O_2 absorption band and multiple H_2O absorption bands. The NIR bandpass includes three H_2O absorption bands at 1.15 , 1.4 , and $1.85 \mu\text{m}$.

3. Results

3.1. The Effect of Volcanism on the Reflectance Spectra

Figure 4 shows the reflectance spectrum of the 30 Gt eruption exoEarth for every six months of the simulation in both a log (upper panel) and linear scale (lower panel). The spectra are shown in units of contrast ratio, which is the radiance of the planet divided by the radiance of the star. Because the stars are much brighter than planets, the contrast ratio of a direct-imaging observation will be lower than 1. However, because we included a coronagraph in our simulated observations, which blocks most of the radiance from the star, the contrast ratio of the spectra in Figure 4 is greater than 1 at certain wavelengths.

The dominant absorber in the UV bandpass is O_3 , which causes the dip at $0.25 \mu\text{m}$ (Figure 4). The volcanic aerosols produced from the eruptions serve as a catalyst for reactions that deplete O_3 , and therefore reduce the amount of light that is absorbed by O_3 . The maximum amount of volcanic aerosols is reached in month 48, which in turn causes the spectrum of month 48 to have the least absorption by O_3 . The eruptions stop after month 48 in the simulation, which allows the O_3 abundance to begin to replenish and the size of the O_3 feature to increase. There is also variation in the slope of the spectra throughout the simulation, where a sharp peak forms around $0.4 \mu\text{m}$ during the first 48 months of the simulation because volcanic aerosols increasingly scatter in the atmosphere. The peak subsides during the last 48 months of the simulation as chemical reactions remove volcanic aerosols from the atmosphere.

The presence of aerosols also affects the O_2 and H_2O absorption features in the VIS bandpass. Because the O_2 abundance was assumed to be constant during the simulation, changes in the O_2 feature are only caused by aerosol scattering

in the upper atmosphere, which conceals the O_2 absorption in the lower atmosphere and decreases the size of the feature. Although the eruptions transport H_2O vapor into the upper atmosphere, the size of the H_2O absorption features in both the VIS and NIR bandpasses are stunted for the first 48 months in the simulations because of the presence of volcanic aerosols. When the eruptions stop, the abundance of volcanic aerosols quickly begins to deplete via chemical reactions, whereas H_2O vapor is removed much more slowly and is able to remain abundant for years after the eruptions. This can be seen in the spectra because the H_2O absorption features remain small during the first 48 months of the simulation, but increase in size during the last 48 months of the simulation (Figure 4).

3.2. Detecting Absorption Features

Using Equation (1), we determined the amount of observation time required to detect ($S/N \geq 5$) the absorption features in the reflectance spectra for each month of every exoEarth simulation. Tables 1–3 list the maximum (Max), minimum (Min), and average (Avg) time for detecting the major features in each bandpass of the four volcanic exoEarth spectra. We considered all 96 spectra for a given exoEarth simulation when determining the Max, Min, and Avg detection time for each feature.

Table 1 lists the observation time needed to detect the O_3 absorption feature in the UV bandpass for the four volcanic exoEarths. The O_3 feature is unique in that it is easily identifiable even when the O_3 absorption is decreased. Furthermore, the feature becomes easier to detect when there is less O_3 absorption because the peak of the feature extends to a higher contrast ratio, which increases the signal of the feature. As a result, the 15, 30, and 60 Gt eruptions have shorter minimum detection times than the 1.8 Gt eruption. For all

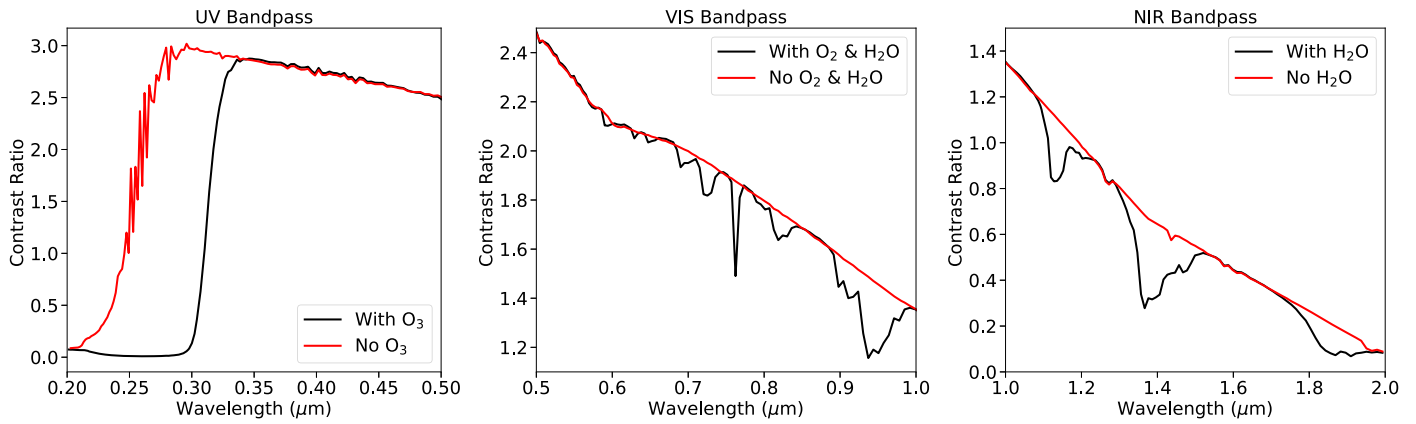


Figure 3. The reflectance spectrum of the 15 Gt eruption exoEarth in month 71 of the simulation with and without absorption from O_3 , H_2O , or O_2 . The left panel shows the UV spectrum without O_3 absorption. The middle panel shows the VIS spectrum without O_2 and H_2O absorption. The right panel shows the NIR spectrum without H_2O absorption.

months in every exoEarth simulation, the O_3 feature required no more than 5 hr of observation to be detected, making it the most consistently detectable feature in any bandpass.

The detectability of the H_2O and O_2 features in the VIS bandpass varies greatly depending on the month in the simulation (Table 2). The maximum time required to detect the H_2O features in the 1.8 Gt case was 224 hr, whereas the maximum for the other three cases all exceed 900 hr. On the other hand, the minimum required observation time is as short as 3 and 6 hr in the 15 Gt and 30 Gt cases, respectively. The minimum detection time for the 1.8 Gt and 60 Gt cases is slightly longer; they require 30 and 37 hr, respectively. Detection of the O_2 feature in the VIS bandpass follows a similar trend, where the feature can require extensive amounts of observation time for a detection in some months, and it may be detected in as little as 18 hr in others. Similar to the H_2O features, the minimum time needed to detect the O_2 feature is shorter for the 15 Gt and 30 Gt cases than for the 1.8 Gt and 60 Gt cases.

The large fluctuation in the detectability of H_2O features is also apparent in the NIR bandpass (Table 3). The features are easiest to detect in the 15 Gt and 30 Gt eruption cases, where they would require 9 and 10 hr of observation, respectively, whereas the H_2O features require 29 hr in the 1.8 Gt case and 33 hr in the 60 Gt case. In all eruption cases, the H_2O features can require a maximum time for detection greater than 180 hr. Although the H_2O features in both the VIS and NIR can require extensive observation time in certain months, the VIS features have shorter minimum observation times because they are at greater contrast ratios and therefore have a stronger signal.

It is interesting to note that the 1.8 Gt and 60 Gt cases have similar minimum detection times for the H_2O features in both the VIS and NIR bandpasses. In all the simulations, the force from the eruptions transports H_2O from the lower atmosphere into the upper atmosphere (Figure 1). In the case of the 30 Gt eruption, the H_2O vapor abundance in the stratosphere increased by three orders of magnitude (Guzewich et al. 2022). This increase in H_2O vapor does not translate into larger H_2O features in the spectra during the first 4 yr of the simulations, however, because the influx of volcanic aerosols enhances scattering and reduces the size of the H_2O absorption features. When the eruptions stop, the volcanic aerosol abundance begins to decrease, which causes the H_2O absorption features to increase in depth over the last 4 yr of

the simulation (Figure 4). The minimum detection time for the H_2O features in every eruption case is achieved during the final year of their simulation, which is when there is the least amount of volcanic aerosols. The larger abundance of volcanic aerosols produced by the 60 Gt eruption takes much longer to deplete than the other eruptions. By the end of the simulation, there are still enough aerosols to significantly impact the size of the H_2O features, which increases their required detection time. The 1.8 Gt eruption produces far fewer volcanic aerosols than the other eruptions, which is why the feature detection time varies far less than for the other eruptions (Tables 1–3). The 1.8 Gt eruption also has the smallest increase in the amount of H_2O vapor in the upper atmosphere, however. As a result, the longer minimum detection times for the H_2O features in the 1.8 Gt case are mainly due to the lower H_2O vapor abundance in the upper atmosphere, and not to the presence of volcanic aerosols.

4. Discussion

4.1. Inferring Volcanism from Reflectance Spectra

A direct detection of SO_2 in the atmosphere of an exoEarth would provide strong evidence of persistent volcanic activity. This is because a consistent flux of SO_2 into the atmosphere would be required in order to sustain detectable amounts of SO_2 , given its short lifetime in an Earth-like atmosphere. Absorption by SO_2 does occur at $0.29 \mu\text{m}$, but it does not appear in the exoEarth spectra because it is overshadowed by O_3 and O_2 absorption (Figure 2). A detection of SO_2 is more plausible in a Venus-like atmosphere given its lack of O_3 and O_2 . An abundance of potential exoVenuses have been discovered (Ostberg & Kane 2019; Ostberg et al. 2023), but their vicinity to their host stars make them poor targets for direct-imaging observations.

Because SO_2 absorption is not visible in the exoEarth spectra, volcanic activity would have to be indirectly inferred by detecting changes in the spectrum that are caused by volcanism. Atmospheric changes caused by seasonal effects can also lead to a change in the size of the absorption features. To determine the magnitude of the spectral changes caused by seasonal effects, we modeled the reflectance spectrum of the baseline exoEarth simulation. This simulation does not include eruptions (Figure 5). The size of the O_3 and O_2 features remains essentially constant throughout the year in the baseline simulation, whereas both features have significant variation in

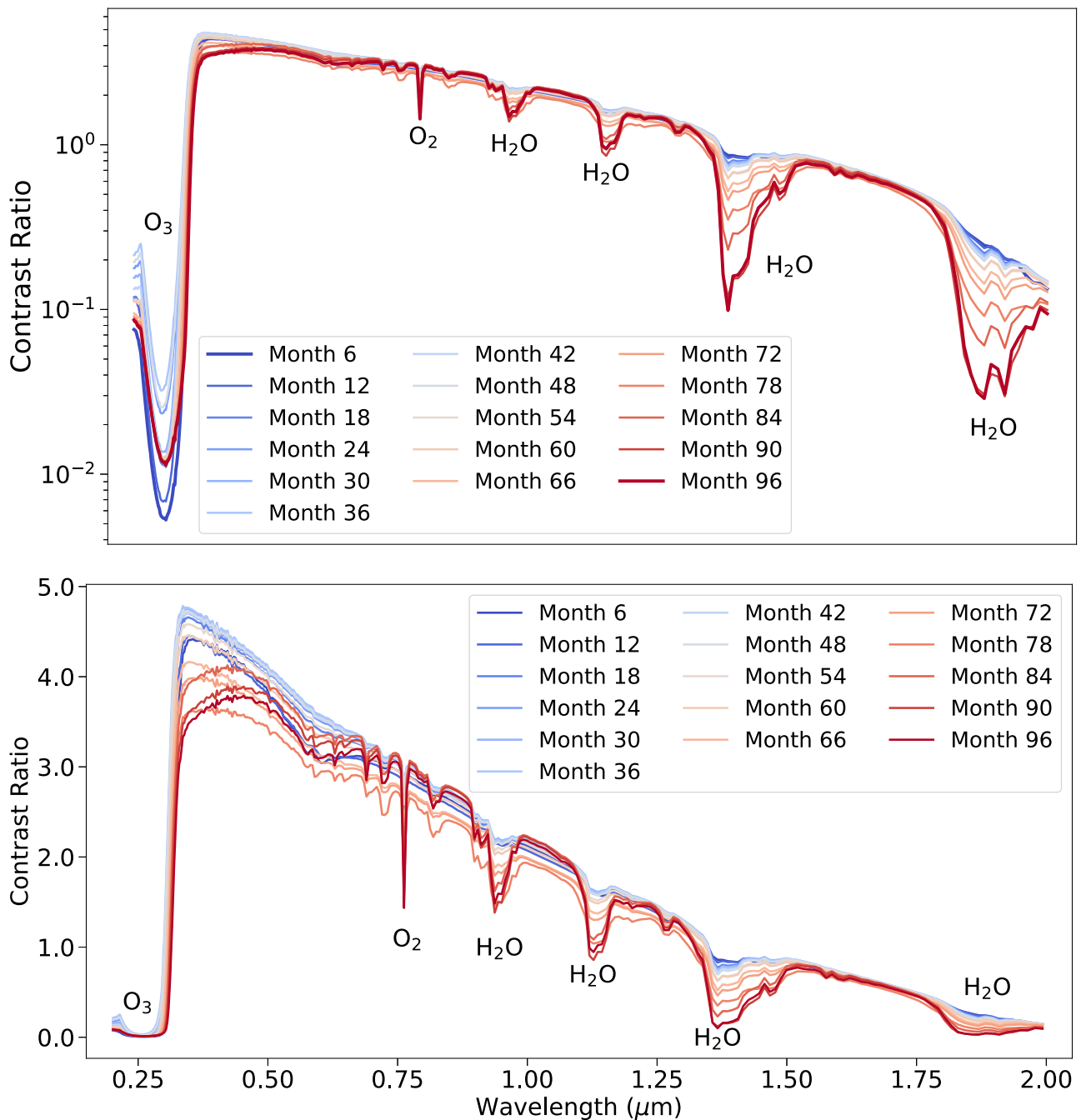


Figure 4. The reflectance spectrum of the 30 Gt eruption exoEarth for every six months of the simulation. Absorption features are labeled with their corresponding molecules. Both panels show the same spectra, but the upper panel is on a log scale, while the lower panel is scaled linearly. There is variation in the size of the O₃ absorption feature and in the slope of the spectra between 0.3 and 0.6 μm due to fluctuations in volcanic aerosol abundance throughout the simulation. The change in slope of the spectrum also affects the location of the continuum. The size of the H₂O features change throughout the simulation because the eruptions cause an influx of volcanic aerosols and H₂O vapor into the upper atmosphere.

Table 1
Observation Hours Required for Detecting O₃ in the UV

Eruption (Gt)	O ₃ Max	O ₃ Min	O ₃ Med
1.8	4	3	3
15	4	2	2
30	4	2	2
60	5	2	2

Note. Max, Min, and Med designate the maximum, minimum, and median time needed to detect the associated feature during each simulation, respectively.

Table 2
Observation Hours Required for Detecting VIS Features

Eruption (Gt)	H ₂ O Max	H ₂ O Min	H ₂ O Avg	O ₂ Max	O ₂ Min	O ₂ Avg
1.8	224	30	107	75	26	37
15	934	3	184	1088	18	297
30	1321	6	185	1139	19	578
60	2939	37	232	1541	26	945

Note. Max, Min, and Med designate the maximum, minimum, and median time needed to detect the associated feature during each simulation, respectively.

Table 3
Observation Hours Required for Detecting NIR Features

Eruption (Gt)	H ₂ O Max	H ₂ O Min	H ₂ O Avg
1.8	182	45	89
15	649	9	124
30	982	10	129
60	2546	42	172

Note. Max, Min, and Med designate the maximum, minimum, and median time needed to detect the associated feature during each simulation, respectively.

the 15 Gt spectra. The H₂O features at 0.95 and 1.15 μm in the baseline spectrum reach the same depth as those in the 15 Gt eruption in month 96, but the H₂O features at 1.35 and 1.85 μm reach a greater depth in the 15 Gt spectra than the baseline spectrum. All H₂O features in the 15 Gt spectra in month 12 are much smaller than those in the baseline spectra because they are almost entirely muted due to the effect of volcanic aerosols.

To avoid potential ambiguity when determining whether spectral changes are caused by seasonal effects or volcanic activity, features that vary significantly more in the volcanic spectra than in the baseline spectrum should be prioritized. To quantify the variation in feature size, we subtracted the minimum contrast ratio from the maximum contrast ratio of every feature in the four volcanic exoEarth cases and in the baseline exoEarth case. The minimum value of a feature was defined to be the lowest contrast ratio achieved by a feature during a given simulation, and the maximum value is the highest contrast ratio achieved by a feature. Both the maximum and minimum values were obtained at the peak wavelength of a given feature. Note that the minimum contrast ratio would be achieved when a feature reached its largest depth.

Table 4 lists the peak wavelength and the maximum change in contrast ratio for the six main features in both the volcanic spectra (Volcanic Diff) and baseline spectrum (Base Diff). We calculated the maximum change of a given feature in all four eruption cases, but only the largest change of the four cases was included in the table. The O₃ feature in the UV changed most in the volcanic spectra during the 60 Gt eruption case, with a maximum change in contrast ratio of 0.0405 (Table 4). The same feature in the baseline spectrum only changes in contrast by 0.0002. In the 30 Gt eruption case, the contrast ratio of the O₂ feature varied by 1.6138, which is the largest variation of the six main features. Unlike the O₃ feature, the O₂ feature varies somewhat in the baseline spectrum, with a maximum difference of 0.3499, but this is still far less than the variation in the O₂ feature in the volcanic spectra (Table 4).

The variation of H₂O decreases toward longer wavelengths in both the volcanic and baseline spectrum, where the H₂O feature at 0.95 μm varies most and the H₂O feature at 1.85 μm varies least (Table 4). In the volcanic spectra, the H₂O features change most in the 15 Gt and 30 Gt eruption cases. The 1.8 Gt case has the lowest variation of all the eruption cases. The H₂O features at 0.95 and 1.15 μm in the 1.8 Gt spectrum vary less than the same features in the baseline spectrum, and they would be indiscernible from the variation caused by seasonal effects.

The O₃ feature in the UV is a potentially viable indicator of volcanism given that the variation in the feature is three orders of magnitude greater in the volcanic spectra than in the baseline spectrum (Table 4). The magnitude of the variation is the smallest of all features, however, meaning that detecting the change in size of the feature would require more sensitive

instrumentation than for the other features. The O₂ feature varies most strongly, and the variation differs most strongly when the variation of the feature in the volcanic spectra is compared to the baseline spectrum. The main downside of the O₂ feature is that it is the thinnest of all the features, and a high spectral resolution is required for a detection. The difference in maximum variation between the volcanic spectra and the baseline spectrum is roughly the same for all H₂O features. However, the H₂O feature in the VIS bandpass at 0.95 μm should be prioritized over the other H₂O features because it varies most strongly (Table 4) and has the best minimum detection time (Table 2).

The sharp peak that forms around 0.4 μm could also be an indicator of volcanism (Figures 4 and 5). The peak only appears in the volcanic spectra and never in the baseline spectrum, which removes any potential ambiguity involved in discerning seasonal and volcanic effects. Unlike using features to infer volcanism, which requires detecting variation across multiple observations, a detection of the peak alone would provide evidence of volcanism and could potentially be made in a single observation. A Venus-like planet that can sustain SO₂ in its atmosphere for an extended period of time could be a potential false positive because it may yield a similar peak in its spectrum.

4.2. Spectral Dependence on the Phase Angle and Observed Longitude

All reflectance spectra were modeled assuming that the illuminated region of the planet facing the observer was at latitude 0° and longitudes 180°–270°, which mostly consists of the Americas and the Pacific Ocean. Changing the illuminated region to include only the Pacific Ocean would likely decrease the average contrast ratio of the spectra because water is less reflective than land. We expect the molecular absorption to be relatively constant between regions because we used monthly averaged atmospheres to model the reflectance spectra.

If we were to compare regional reflectance spectra on shorter timescales, then we would expect there to be spectral differences because of localized weather patterns and cloud coverage. In addition, the cadence of the observations could cause the phase and illuminated region of the planet to differ in each observation. These variations in weather and viewing geometry can lead to discrepancies in the reflectance spectra from separate observations. It should be investigated in future studies whether these spectral variations are distinguishable from those caused by volcanism to confirm whether changes in absorption features can be a reliable indicator of volcanic activity.

4.3. Likelihood of Observing an ExoEarth with Ongoing Volcanism

Detection of signs of volcanic activity in an exoplanet atmosphere requires observations to be conducted while volcanism is occurring on the planet, or while the atmosphere still has remnants of past volcanism. The frequency of LIP volcanism on Earth has varied throughout time. From the present day to 180 Mya, LIPs occurred about once every 10 My (Coffin & Eldholm 2001; Ernst et al. 2005), but from 180 to 2600 Mya, LIPs occurred once every 20 My (Ernst 2014). The time for which an LIP remains active can be as long as tens of millions of years, but most cases of LIPs are shorter and last

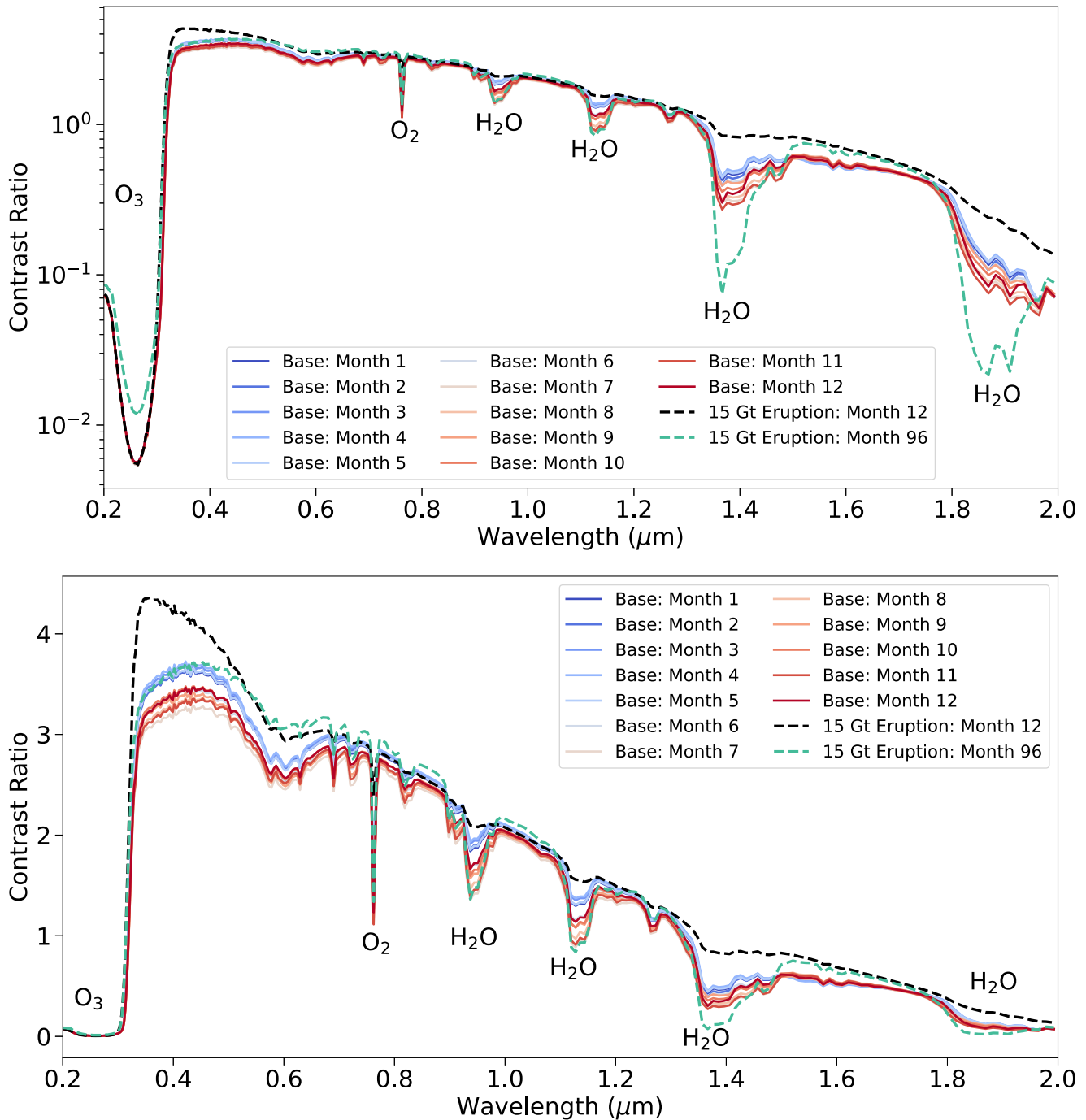


Figure 5. The reflectance spectra for each month of the baseline exoEarth simulation in comparison to months 12 and 96 of the 15 Gt eruption. Both plots show the same spectra, but the upper panel is on a log scale, and the lower panel is scaled linearly.

only 0.5–1.0 My (Hofmann et al. 2000; Courtillot & Renne 2003; Jerram & Widdowson 2005; Blackburn et al. 2013; Ernst 2014).

We assumed that on average, LIPs on Earth have occurred every 15 million years and lasted for 1 million years. This means that if one were to choose a random year over the last 3 Gy of Earth’s history, the chance of an active LP is approximately 6.6%. when we assume that exoEarths targeted in future direct-imaging missions also have a 6.6% chance of having an active LIP, then at least 47 planets would need to be observed for a chance greater than 90% that at least one planet has ongoing volcanism. This is an optimistic first-order

approximation because it is contingent on a variety of assumptions, but it demonstrates that a significant amount of observing time is required for an opportunity to detect volcanism on an exoplanet.

5. Conclusions

In this work, we explored the possibility of detecting volcanism in the reflectance spectrum of an exact exoEarth analog orbiting a Sun-like star at 1 au. The primary absorption features in the reflectance spectra were O_3 in the UV bandpass, O_2 and H_2O in the VIS bandpass, and H_2O in the NIR

Table 4
Variation in the Feature Contrast Ratio

Feature	Peak Wavelength	Volcanic Diff	Baseline Diff
O ₃	0.25	0.0405	0.0002
O ₂	0.75	1.6138	0.3499
H ₂ O	0.95	1.3948	0.5813
H ₂ O	1.15	1.1411	0.4857
H ₂ O	1.35	0.8064	0.1795
H ₂ O	1.85	0.1815	0.0373

Note. The maximum change in contrast ratio for the main features in the four volcanic exoEarth spectra (Volcanic Diff), and the baseline exoEarth spectrum with no eruptions (Baseline Diff).

bandpass. We determined the range of detectability for each absorption feature in all reflectance spectra for all four eruption cases. Absorption by O₃ was both the easiest to detect and the most consistently detectable feature of the group because absorption was always present in every spectrum. The detectability of every other feature varied greatly on a monthly basis. In particular, the H₂O absorption features were almost entirely concealed by volcanic aerosols while eruptions were ongoing, and they continuously grew in size when the eruptions ceased and the volcanic aerosols began to be removed from the atmosphere.

Detecting SO₂ in the atmosphere of an exoEarth would provide strong evidence for ongoing volcanism given the short lifetime of SO₂ in Earth's atmosphere. While eruptions were ongoing in the simulations, absorption by SO₂ contributed to the reflectance spectra, but was always hidden beneath the stronger O₃ absorption feature that appears around 0.3 μm . Because SO₂ absorption is undetectable in the simulated exoEarth spectra, we propose that the best method for inferring volcanism is through detecting spectral changes caused by volcanism, or by observing the sharp peak that forms between 0.3 and 0.5 μm .

We quantified the maximum amount of variation incurred by each of the major features in the reflectance spectra of each of the volcanic exoEarths and the baseline exoEarth. The maximum variation of every feature in the volcanic spectra was greater than the variation of the same features in the baseline spectrum. The case of the 1.8 Gt eruption spectra was the only eruption case with features with less variation than the baseline spectrum. These were the H₂O features at 0.95 and 1.15 μm . The O₃ feature and O₂ and H₂O features in the VIS bandpass have the largest discrepancy in variation between the volcanic and baseline spectrum, making them optimal features for discerning spectral changes caused by volcanism from those caused by seasonal effects. The sharp peak that forms in the volcanic spectra between 0.3 and 0.5 μm is also a potentially strong indicator of ongoing volcanism because it only formed during times of high volcanic aerosol abundance.

Future work is required to investigate whether short-term changes in weather or cloud coverage may cause fluctuations in spectral features similar to those caused by volcanism. If the changes in spectra features from weather and volcanism are similar, then changes in feature size alone may not be a reliable indicator of ongoing volcanism. This work considered a small wavelength range, but other wavelength ranges should be investigated to determine whether other volcanic indicators, such as absorption by SO₂, could be detected in other bandpasses. Eruptions of different compositions should be










tested as well to determine whether some eruptions may be easier to detect than others. Modeling eruptions similar to the Hunga Tonga eruption, which delivered massive amounts of H₂O vapor into the atmosphere, may have a far more significant effect on H₂O absorption features and could prove to be a more reliable signal than what we discussed in this work.

Direct-imaging missions will be our first opportunity to characterize the atmospheres of exoEarths around Sun-like stars. These missions are planned to be launched in at least the next decade, but in the meantime, it is vital that we refine our ability to analyze such data so that we may maximize what can be learned from them. In particular, learning how to identify possible indicators of volcanism on an exoplanet will be crucial because it can provide invaluable insight into the state of the planet's interior, which otherwise is inaccessible to us. Improving our understanding of volcanic outgassing within the solar system is also important, so that we may better infer the likelihood of volcanism on exoplanets (Horner et al. 2020; Kane et al. 2021). These parallel data sources will help improve our understanding of the different evolutionary pathways of terrestrial planets, and they may potentially identify the planets that may have surface conditions suitable for life.

Acknowledgments

Ostberg and Kohler were supported by the NASA Deep Atmosphere Venus Investigation of Noble gases, Chemistry, and Imaging (DAVINCI) mission. Guzewich, Oman, Fauchez, Kopparapu, Richardson, and Whelley were supported by NASA GSFC's Sellers Exoplanet Environments Collaboration. Kane was supported by NASA grant 80NSSC21K1797, funded through the NASA Habitable Worlds Program. GEOSCCM is supported by the NASA MAP program, and the high-performance computing resources were provided by the NASA Center for Climate Simulation (NCCS). The material is based upon work supported by NASA under award number 80GSFC21M0002.

ORCID iDs

Colby M. Ostberg  <https://orcid.org/0000-0001-7968-0309>
 Scott D. Guzewich  <https://orcid.org/0000-0003-1149-7385>
 Stephen R. Kane  <https://orcid.org/0000-0002-7084-0529>
 Erika Kohler  <https://orcid.org/0000-0002-0000-199X>
 Luke D. Oman  <https://orcid.org/0000-0002-5487-2598>
 Thomas J. Fauchez  <https://orcid.org/0000-0002-5967-9631>
 Ravi K. Kopparapu  <https://orcid.org/0000-0002-5893-2471>
 Jacob Richardson  <https://orcid.org/0000-0002-1736-8907>
 Patrick Whelley  <https://orcid.org/0000-0003-3266-9772>

References

- Aquila, V., Baldwin, C., Mukherjee, N., et al. 2021, *JGRD*, **126**, e2021JD034830
- Bean, J. L., Stevenson, K. B., Batalha, N. M., et al. 2018, *PASP*, **130**, 114402
- Beichman, C., Benneke, B., Knutson, H., et al. 2014, *PASP*, **126**, 1134
- Blackburn, T. J., Olsen, P. E., Bowring, S. A., et al. 2013, *Sci*, **340**, 941
- Bond, D. P., & Sun, Y. 2021, in *Large Igneous Provinces: A Driver of Global Environmental and Biotic Changes*, ed. R. Ernst, A. Dickson, & A. Bekker (New York: Wiley), 83
- Bryan, S. E., Peate, I. U., Peate, D. W., et al. 2010, *ESRv*, **102**, 207
- Checlair, J. H., Villanueva, G. L., Hayworth, B. P., et al. 2021, *AJ*, **161**, 150
- Coffin, M. F., & Eldholm, O. 2001, in *Mantle Plumes: Their Identification through Time*, ed. R. Ernst & K. Buchan (Boulder, CO: Geological Society of America), 59

- Colarco, P., da Silva, A., Chin, M., & Diehl, T. 2010, *JGRD*, **115**, D14207
- Courtillot, V. E., & Renne, P. R. 2003, *CRGeo*, **335**, 113
- Duncan, B., Strahan, S., Yoshida, Y., Steenrod, S., & Livesey, N. 2007, *ACP*, **7**, 3713
- Ernst, R. E. 2014, *Large Igneous Provinces* (Cambridge: Cambridge Univ. Press)
- Ernst, R. E., Buchan, K. L., & Campbell, I. H. 2005, *Litho*, **79**, 271
- Faucher, T. J., Turbet, M., Sergeev, D. E., et al. 2021, *PSJ*, **2**, 106
- Felton, R. C., Bastelberger, S. T., Mandt, K. E., et al. 2022, *JGRE*, **127**, e2021JE006853
- Fortenbach, C. D., & Dressing, C. D. 2020, *PASP*, **132**, 054501
- Fortin, M.-A., Gazel, E., Kaltenecker, L., & Holecross, M. E. 2022, *MNRAS*, **516**, 4569
- Fraine, J., Deming, D., Benneke, B., et al. 2014, *Natur*, **513**, 526
- Gaudi, B. S., Seager, S., Mennesson, B., et al. 2020, arXiv:2001.06683
- Greene, T. P., Bell, T. J., Ducrot, E., et al. 2023, *Natur*, **618**, 39
- Greene, T. P., Line, M. R., Montero, C., et al. 2016, *ApJ*, **817**, 17
- Guenther, E. W., & Kislyakova, K. G. 2020, *MNRAS*, **491**, 3974
- Guzewich, S. D., Oman, L. D., Richardson, J. A., et al. 2022, *GeoRL*, **49**, e2021GL096612
- Harnett, C. E., Heap, M. J., & Thomas, M. E. 2020, *P&SS*, **180**, 104762
- Head, J. W., Chapman, C. R., Strom, R. G., et al. 2011, *Sci*, **333**, 1853
- Hofmann, C., Feraud, G., & Courtillot, V. 2000, *E&PSL*, **180**, 13
- Horner, J., Kane, S. R., Marshall, J. P., et al. 2020, *PASP*, **132**, 102001
- Hu, R., Seager, S., & Bains, W. 2013, *ApJ*, **769**, 6
- Jaeger, W. L., Keszthelyi, L. P., Skinner, J., Jr., et al. 2010, *Icar*, **205**, 230
- Jerram, D. A., & Widdowson, M. 2005, *Litho*, **79**, 385
- Kaltenecker, L., Henning, W., & Sasselov, D. 2010, *AJ*, **140**, 1370
- Kane, S. R., Arney, G. N., Byrne, P. K., et al. 2021, *JGRE*, **126**, e06643
- Kane, S. R., Roettenbacher, R. M., Unterborn, C. T., Foley, B. J., & Hill, M. L. 2020, *PSJ*, **1**, 36
- Kasbohm, J., & Schoene, B. 2018, *SciA*, **4**, eaat8223
- Kislyakova, K. G., Noack, L., Johnstone, C. P., et al. 2017, *NatAs*, **1**, 878
- Kopparapu, R., Arney, G., Haqq-Misra, J., Lustig-Yaeger, J., & Villanueva, G. 2021, *ApJ*, **908**, 164
- Kreidberg, L., Koll, D. D. B., Morley, C., et al. 2019, *Natur*, **573**, 87
- Krissansen-Totton, J., Olson, S., & Catling, D. C. 2018, *SciA*, **4**, eaao5747
- Krissansen-Totton, J., Thompson, M., Galloway, M. L., & Fortney, J. J. 2022, *NatAs*, **6**, 189
- Lancaster, M. G., Guest, J. E., & Magee, K. P. 1995, *Icar*, **118**, 69
- Loftus, K., Wordsworth, R. D., & Morley, C. V. 2019, *ApJ*, **887**, 231
- Lustig-Yaeger, J., Meadows, V. S., & Lincowski, A. P. 2019, *AJ*, **158**, 27
- Madhusudhan, N. 2019, *ARA&A*, **57**, 617
- McKay, D. I. A., Tyrrell, T., Wilson, P. A., & Foster, G. L. 2014, *E&PSL*, **403**, 254
- Misra, A., Krissansen-Totton, J., Koehler, M. C., & Sholes, S. 2015, *AsBio*, **15**, 462
- Nielsen, J. E., Pawson, S., Molod, A., et al. 2017, *JAMES*, **9**, 3019
- Noack, L., Kislyakova, K. G., Johnstone, C. P., Güdel, M., & Fossati, L. 2021, *A&A*, **651**, A103
- O'hara, M. 2000, *JPet*, **41**, 1121
- Oppenheimer, C. 2002, *QSRv*, **21**, 1593
- Ostberg, C., & Kane, S. R. 2019, *AJ*, **158**, 195
- Ostberg, C., Kane, S. R., Li, Z., et al. 2023, *AJ*, **165**, 168
- Pidhorodetska, D., Faucher, T. J., Villanueva, G. L., Domagal-Goldman, S. D., & Kopparapu, R. K. 2020, *ApJL*, **898**, L33
- Quanz, S. P., Ottiger, M., Fontanet, E., et al. 2022, *A&A*, **664**, A21
- Quick, L. C., Roberge, A., Mlinar, A. B., & Hedman, M. M. 2020, *PASP*, **132**, 084402
- Ridden-Harper, A., Nugroho, S. K., Flagg, L., et al. 2023, *AJ*, **165**, 170
- Rienecker, M., Suarez, M. J., Todling, R., et al. 2008, NASA Technical Report TM-2007, NASA
- Seager, S., & Deming, D. 2010, *ARA&A*, **48**, 631
- Self, S., Widdowson, M., Thordarson, T., & Jay, A. E. 2006, *E&PSL*, **248**, 518
- Sing, D. K., Pont, F., Aigrain, S., et al. 2011, *MNRAS*, **416**, 1443
- Stoiber, R. E., & Jepsen, A. 1973, *Sci*, **182**, 577
- Stothers, R. B. 1984, *Sci*, **224**, 1191
- Strahan, S., Duncan, B., & Hoor, P. 2007, *ACP*, **7**, 2435
- The LUVUOIR Team, et al. 2019, arXiv:1912.06219
- Thompson, M. A., Krissansen-Totton, J., Wogan, N., Telus, M., & Fortney, J. J. 2022, PNAS, **119**, e2117933119
- Tinetti, G., Deroo, P., Swain, M., et al. 2010, *ApJL*, **712**, L139
- Turbet, M., Bolmont, E., Leconte, J., et al. 2018, *A&A*, **612**, A86
- Turbet, M., Leconte, J., Selsis, F., et al. 2016, *A&A*, **596**, A112
- Wolf, E. T. 2017, *ApJL*, **839**, L1
- Wolf, E. T., Shields, A. L., Kopparapu, R. K., Haqq-Misra, J., & Toon, O. B. 2017, *ApJ*, **837**, 107